Wetting of mesoscopic soft cylinders: Structure and layering transitions

Heiko Ahrens, Norbert Hugenberg, Manfred Schmidt, and Christiane A. Helm*
Institut für Physikalische Chemie, Johannes Gutenberg-Universität, Jakob-Welder Weg 11, D-55099 Mainz, Germany
(Received 21 December 1998; revised manuscript received 26 May 1999)

The wetting of soft mesoscopic long-chain particles is studied. As a model system, a cylindrical brush with poly(vinyl)pyridine side chains on the water surface is characterized by isotherms and x-ray reflectivity. The forces from the two planar interfaces and the intra- and interparticle interactions are all of comparable magnitude. Two layering transitions occur, one from the monolayer to the double layer, the next to a homogeneous multilayer. The hard wall from which layering starts is the smooth polymer/air interface. Indeed, they particles in the top layer of both the double- and the multilayer have their cylinder axis parallel to the surface and are laterally compressed. In contrast, the polymer/water interface is diffuse due to brush swelling. Generally, the long-chain particles adjacent to the respective interfaces do not maintain their circular diameters. The thickness of the monolayer can be varied by a factor 3.5, up to 53 Å. An additional phase transition occurs within the monolayer, which is attributed to a change of the side chains from a flattened to a compressed state at constant volume. Atmoic force microscope images of the monolayer transferred onto a solid indicate local cylinder alignment. [S1063-651X(99)03710-1]

PACS number(s): 68.10.−m

INTRODUCTION

The identification and sophisticated use of distinct and common features of different classes of soft systems may hold the key to the design of new materials with desired intermediate properties. This represents one of the most formidable challenges in soft condensed-matter physics [1]. Thus molecules, colloids, or supramolecular assemblies with a defined symmetrical topology (like spheres, cylinders, or lamellae) exhibit common structural features, even though the systems may differ by 4 orders of magnitude in size [2–5]. These interactions of purely geometric origin have also been found in theoretical calculations as well as computer simulations [6–9]. The topology effect is especially prominent in a confined geometry or adjacent to a hard and smooth surface, since quasilayering occurs. Thus, perpendicular to the interface, the density profile oscillates with a periodicity correlated to the size of the system (like the sphere or cylinder diameter or the lamella thickness [2]). Apart from its obvious scientific interest, the structure close to an interface is also of technical relevance, since it controls adhesion, wetting, and function such as optical and electrical properties [10].

Unfortunately, the simplest experimental approach, investigating a liquid-gas interface, fails for most systems. Only if the roughness of a liquid surface is smaller than the system dimension, layering occurs (cf. Fig. 1). There are very few examples: atomic fluids like liquid gallium [11] or mercury [3] exhibit an extremely high surface tension, which decreases the capillary-wave amplitudes below the atomic diameter. The other known systems are supramolecular assemblies like micelles [12], as well as layers from amphophilic molecules in the L_α phase [13] or liquid crystals in the smectic phase [14].

When topology effects are considered, the systems are usually assumed to be hard spheres or long-chain molecules (the latter with a constant diameter and a finite persistence length). This assumption is certainly valid for atoms, linear polymers in a melt, or colloids [3–5]. The dominance of topology is easily understood if the range of interparticle forces is small compared to particle size. This, however, is different if the particle itself is soft and hence may change its shape or if the forces are long ranged. For instance, supramolecular assemblies like micelles or bilayers are soft. Indeed, the experimental evidence suggests surface-induced size changes of micelles [12]; also, stress-induced orientation effects of molecules within a lamella are reported [10,15,16]. Furthermore, apparently simple questions are not yet resolved, for instance, how large an aggregate nucleating an additional layer has to be.

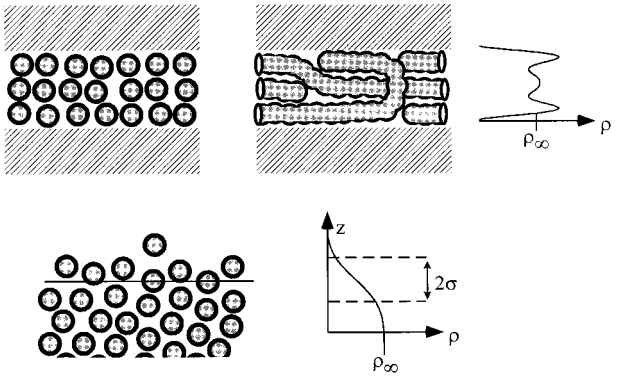

FIG. 1. Top: A spherical and a long-chain system confined between smooth walls separated by three molecular diameters together with a schematic density profile [2]. Bottom: A liquid/gaseous interface where the roughness σ (drawn to scale) and the sphere diameter are comparable.

*Author to whom correspondence should be addressed. Present address: Fachbereich Physik der Universität des Saarlandes, Fachrichtung 10.2–Strukturforschung, Postfach 151150, Bau 9.1, 66041 Saarbrücken, Germany. Electronic address: chelm@mail.uni-mainz.de

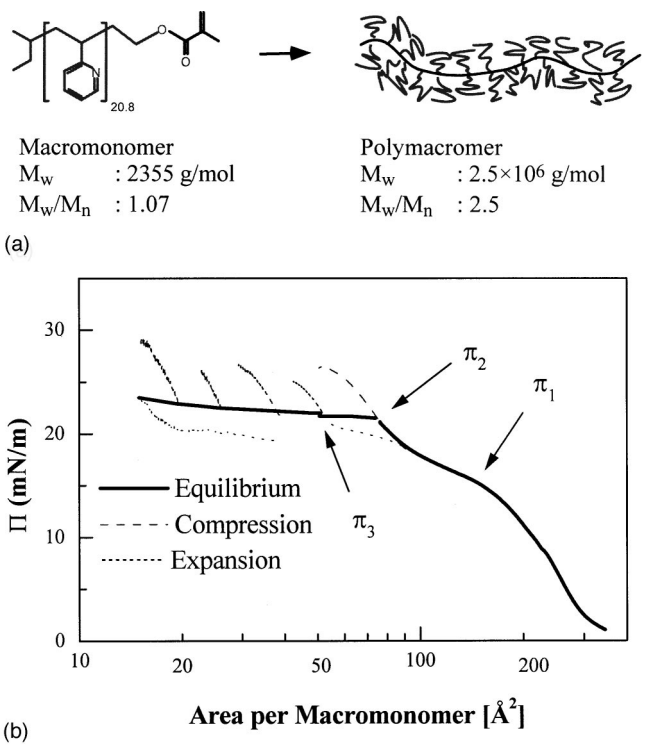

FIG. 2. (a) Structural formula of the cylindrical brush obtained by polymerization of polymacromonomers. (b) Equilibrium isotherm. Dashed lines indicate compression, dotted lines expansion [16 Å^2/(macromonomer×min)]. Beyond π_3, stopping the barrier leads to pressure relaxation (decrease on compression, increase on expansion, respectively) towards the equilibrium isotherm.

It would be desirable to distinguish the influence of the system topology from interfacial and intramolecular interactions. Yet, the intermediate behavior of a soft colloid has been virtually unexplored, mainly due to the lack of model systems. With the advent of polymers with complex architectural molecules have become available with supramolecular mesoscopic characteristics [17–19]. These systems present a challenge, mainly because of the potential to combine the local properties of a polymer melt with supramolecular mesoscopic interfacial characteristics. Thus, not only layering transitions may occur in the phase diagram but also phase transitions correlated with the arrangement of the tethered polymer [20].

We observe the layering transition by laterally compressing a polymer on the surface of a Langmuir trough. From isotherms, we obtain the phase diagram [21,22] and from x-ray reflectivity [23,24] the thickness, and thus the layer deformation [15,16].

The recent success of macromolecular chemistry in synthesizing cylindrical brushes with monodisperse side arms [17] has provided the necessary tools for addressing the above problems. These macromolecules (cf. Fig. 2) consist of linear homopolymer arms (side chains) covalently bound to each repeating unit of the main chain forming the core of the cylinder. The degree of polymerization of the main chain exceeds the one of the side chains substantially. The homopolymer arms are poly(vinyl)pyridine (PVP), which is suitable because linear chain PVP forms insoluble and compressible monolayers at the air/water interface [25]. Since bulk PVP is in the glassy phase, the fluidity of the PVP monolayer is probably due to solvent incorporation [26] as well as to film thinning [27].

I. EXPERIMENT AND ANALYSIS

Cylindrical brushes consisting of PVP side chains bound to a methacrylate main chain were synthesized by radical polymerization of PVP macromonomers described elsewhere [17] [cf. Fig. 2(a)]. Due to the large one-dimensional anchoring density (1/2.5 Å^{-1}) the side chains are stretched, leading to a large persistence length of the cylinder. Actually, for similar cylindrical brushes with poly(styrene) side chains a persistence length of ≈1000 Å was found [17].

Chloroform solutions of the cylindrical brushes were spread on pure water. Isotherms were measured on a Langmuir trough with a Wilhelmy system (R&K, Wiesbaden, Germany). The specular x-ray scattering on liquid surfaces was performed with a homemade θ–θ setup described elsewhere [28] ($U=40$ kV, $I=55$ mA, and $\lambda=1.54$ Å; the system acts as a two-circle diffractometer with unusual geometry. Both the x-ray tube and detector are attached to a goniometer, which can be moved vertically by a lifting jack. In this geometry, detector and source are rotated in opposite directions with the same angle θ). All x-ray reflectivity measurements at the air/water interface are performed at 20 °C. The films were stable during the reflectivity measurements, which take from 2 to 15 h. The data are background corrected. For AFM imaging (Digital IIIa), the monolayers were transferred onto silicon wavers by a motorized dipper. To monitor possible changes occurring during or after film transfer onto solid support, additional x-ray scattering was performed (Siemens D-500).

Specular reflection of x rays provides information on the electron-density variation perpendicular to the surface with Å resolution. For x rays with a wavelength of $\lambda=1.54$ Å, the index of refraction depends only on the electron density ρ and various constants (Thompson radius $r_0=2.8\times10^{-5}$ Å),

$$n=1-r_0\rho\lambda^2/2\pi. \tag{1}$$

The reflectivity can be seen as the Fresnel reflectivity R_F of an infinitely sharp interface modulated by interference effects from the thin surface layer. The refractive index is only slightly less (ca. 10^{-5}) than 1. Therefore, dynamic effects (e.g., multiple scattering or beam refraction) contribute significantly to the reflectivity R only at small angles of incidence. Above about two critical angles the reflectivity can be described by the kinematic approximation [14,29],

$$\frac{R}{R_F}=\left|\frac{1}{\rho_{\mathrm{sub}}}\int \rho'(z)e^{iQ_z z}dz\right|^2, \tag{2}$$

where ρ_{sub} is the electron density of the bulk phase [$\rho_{\mathrm{sub}}(\mathrm{water})=0.333e^-/\text{Å}^3$], $\rho'(z)$ is the gradient of the electron density along the surface normal, and Q_z is the wave-vector transfer normal to the surface. Due to the loss of the phase information in conventional x-ray reflectivity experiments the data analysis is generally based on finding proper electron-density functions whose reflectivity properties retrospectively best match the observed reflectivity data.

To obtain the optimum interfacial electron-density variations we used two different strategies.

(i) The layer is subdivided into homogenous slabs (box model) [23,24]. Each box is parametrized by a length and an electron density. The transition between adjacent boxes is smoothed. Proper smearing parameters describe the interfacial roughness (the roughness has the same effect as the Debye-Waller factor; it damps the interference maxima at large Q_z). The parameters are determined by a least-squares method. Box models are convenient because they can easily be applied to Eq. (2) and individual boxes may be identified with certain structural properties of the layers. For more complex electron-density profiles however, many boxes are necessary to suitably describe the experimental data. This necessitates the determination of more adjustable parameters than one can unambiguously deduce from the reflectivity data, and various sets of parameters may result in the same electron-density profile within the experimental error [28,30] To recognize coupled parameters an interdependency analysis is performed [31].

(ii) The electron-density profile is determined with a model-independent method [32,33]. From the experimentally observed reflectivity curve the corresponding profile correlation function is estimated via indirect Fourier transformation. For this profile correlation function the matching scattering-length density profile is then derived by square-root deconvolution. Both the correlation function and the density profile are expressed in terms of a linear combination of a set of suitable basis functions. The number of basis functions, and thus, that of free parameters, can be optimized (minimized) by a smoothness criterion for the correlation function and, in most cases, no *a priori* assumptions on the shape of the electron-density profile have to be made.

Our interpretation of the reflectivity data was considered satisfactory when the scattering density profiles resulting from the two different modeling processes were equivalent. To obtain structural parameters characterizing one phase, we used the box model with the fewest and most independent parameters with all reflectivity curves measured in this phase could be fitted satisfactorily.

II. EXPERIMENTAL RESULTS

A. Isotherms

Figure 2(b) presents the pressure-area isotherm on a water surface at 20 °C. Nonzero pressure occurs at about a 300 Å^2/macromonomer, at π_1 (150 Å^2/macromonomer) an pronounced slope change indicates a phase transition [34]. Additional slope changes at π_2 (85 Å^2/macromonomer) and π_3 (40–50 Å^2/macromonomer) are observed. The shape of the isotherm is reminiscent of successive multilayer formation [6,21,22,35]. Up to π_2, the isotherm is reversible and independent of compression speed.

Yet, in the compressed film dynamics are slow. Therefore, in the isotherm [cf. Fig. 2(b)] beyond π_3 the equilibrium pressure is shown, which is obtained after a few hours of relaxation. This equilibrium pressure is smaller than the dynamical compression pressure (measured with a moving barrier), but larger than the dynamical expansion pressure. Above π_3, the equilibrium π-A diagram is measured by stopping the barrier several times during a compression run. Independent of the molecular area, a pressure increase occurs on compression ($v = 0.067$ Å^2/(macromonomer×min). The relaxation slows drastically when the area per macromonomer approaches 10 Å^2.

In contrast, between π_2 and π_3, the pressure is constant. This is indicative of a coexistence range between two phases. Actually, as will be shown further below, a mono- and double layer of cylindrical brushes coexist. The kinetic behavior is similar to the one observed at π_3, yet the velocities involved are two orders of magnitude faster. However, at compression speeds larger than 10.6 Å^2/(macromonomer×min) the sharp pressure increase just before π_2, but leads to immediate and irreversible film collapse. At lower velocities, a pressure overshoot occurs at the phase transition, which levels off to the equilibrium value. Such a dynamic behavior is typical for layering transitions [21].

The equilibrium isotherm depends only weakly on temperature. Much more obvious is the effect of the temperature on the film dynamics. Qualitatively, for π_2 a temperature decrease has the same effect as a speed increase. Obviously, a high activation energy is necessary to squeeze cylindrical brushes out of the monolayer to form a double layer.

B. X-ray reflectivity of the monolayer

Figure 3(a) shows the x-ray reflectivity curves of the monolayer up to π_2. The curves measured at the expanded monolayer below π_1 show only one maximum, indicating at least one very rough interface. On compression, the maximum shifts to lower Q_z, a sign of film thickening. Since there is so little structure, a one-box model is sufficient to describe the electron-density profiles [cf. Fig. 3(b)]. The parameters are (cf. Table I) length l_1, electron density ρ_1, and two smearing parameters for the air/polymer and the polymer/water interface, $\sigma_{\mathrm{air/pol}}$ and $\sigma_{\mathrm{pol/w}}$, respectively. As shown in Figs. 4 and 5, the electron density is basically constant, while the thickness increases from 15 to ≈30 Å.

On compression, the brushes deform, yet they do not dehydrate. This can be best seen in Fig. 4(a), where the thickness $l = l_1$ (cf. Table I) as a function of the lateral macromonomer density $1/A$ (i.e., the inverse area per macromonomer) is shown. The linear increase of the thickness indicates a constant volume of $V = 4320$ Å^3 per macromonomer (within 15% error). Multiplying the volume V with the experimentally measured electron density ρ_1 (which is basically constant), one obtains the amount of electrons per macromonomer, $N_e = A\rho l = 1606e^-$. If one compares this number with the one calculated from the structure formula ($1258e^-$), one finds that each macromonomer has 346 extra electrons, or 1.6 water molecules per pyridine group. With the molecular water volume, 30 Å^3, one obtains for the dry volume per macromonomer 3275 Å^3. From these values, the mass density of the dry polymer is calculated (1.19 g/cm^3), which is found to be slightly higher than the value reported in the literature (1.15 g/cm^3) [36], indicating that the voids of the melt are filled with water leading to a more efficient packing at the interface [26].

On the first increase of lateral pressure, the film height amounts to 15 Å, about 1.5 times the cross-sectional area of the PVP side chain (≈10±2 Å [37]). This finding is consis-

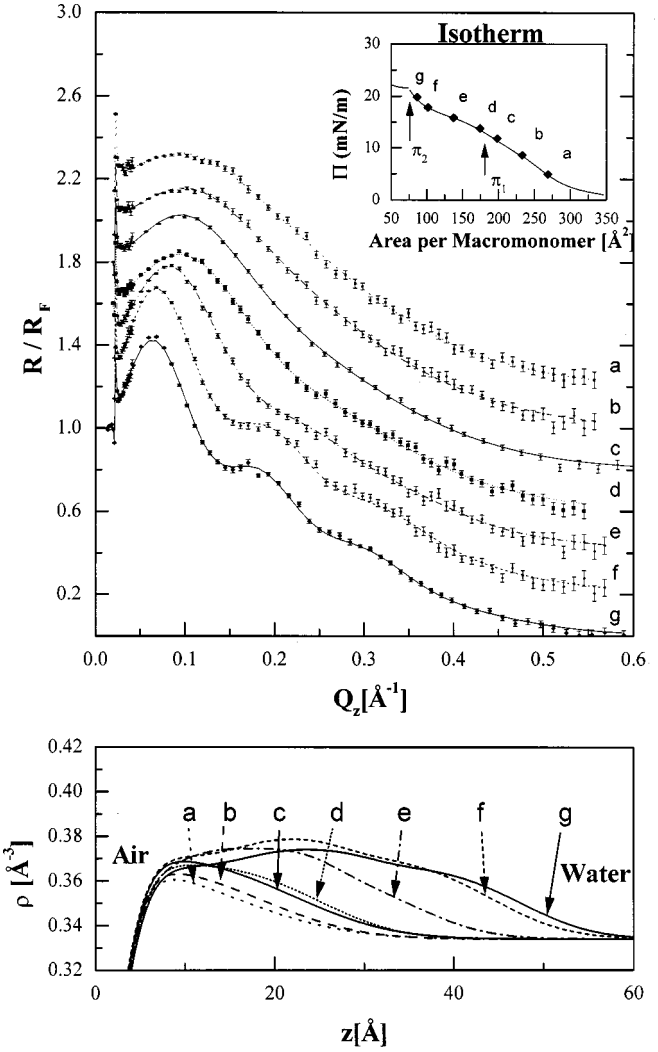

FIG. 3. Top Normalized x-ray reflectivity of the monolayer taken along the isotherm (shown in the inset) up to π_2 at different molecular areas. For clarity, each curve is displaced by 0.2. The full lines are simulated curves from which the electron-density profile shown at the bottom is calculated.

tent with the molecular structure: Every $h=2.5$ Å a macromonomer with a contour length of $r_{max}=62$ Å is attached to the main chain. Thus, the maximum diameter of the flattened ''cylindrical'' brushes is $2r_{max}=124$ Å, corresponding to $2r_{max}h=310$ Å^2/macromonomer. Actually, already at 330 Å^2/macromonomer the pressure is nonzero, a fact probably

TABLE I. Up to π_1 the electron-density profile of the monolayer is parametrized as a one-box model with electron density ρ_1 and length l_1. $\sigma_{air/w}$ and $\sigma_{pol/w}$ describe the roughness at the air/water and the polymer/water interface, respectively. π_1 occurs between measurements ''d'' and ''*e*'' at ≈150 Å^2/macromonomer.

	Area (Å^2)	Length l_1 (Å)	ρ_1/ρ_{water}	$\sigma_{air/w}$ (Å)	$\sigma_{pol/w}$ (Å)
a	268.5	15.02	1.114	3.292	10.07
b	232.9	18.68	1.103	3.282	8.403
c	197.7	22.01	1.115	3.321	8.694
d	174.1	24.88	1.102	3.4	7.131
e	137.1	32.71	1.116	3.448	7.087

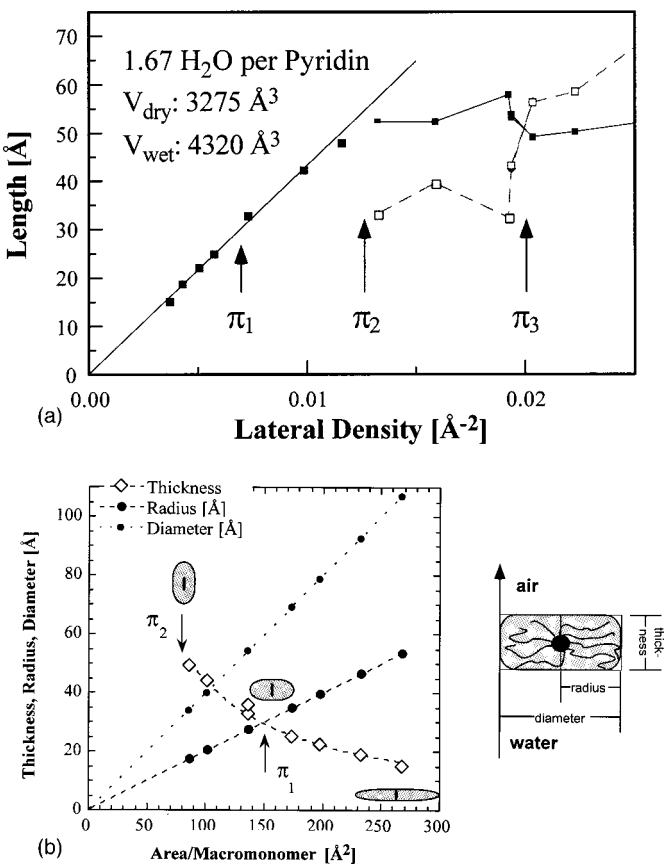

FIG. 4. (a) Thickness of the top monolayer as a function of the lateral density per macromonomer (calculated in the respective phases according to the following: for $\pi<\pi_1$, l_1 from Table I; for $\pi_1<\pi<\pi_2$, l_{sum} from Table II; and for $\pi_2<\pi$, l_{mono} from Tables III and IV), as well as the thickness of the second monolayer during double layer buildup (for $\pi>\pi_2$). Full symbols correspond to the top monolayer, open symbols correspond to the bottom monolayer. (b) The average height, radius, and diameter of the ''cylindrical'' particles as a function of area per macromonomer.

due to the arbitrary in-plane distribution of the ''cylindrical'' brushes. Thus, below π_1 the ''cylindrical'' brush resembles a centipede with most legs spread, a few legs sit on top of each other, all are swollen by water. While in the bulk phase the ''cylindrical'' brushes actually have a cylindrical cross section, the monolayer below π_1 consists of flat ellipsoids.

The structural data from the monolayer on the water surface agree well with those obtained from the same PVP polymacromers spin coated on mica. There, a diameter of $2r=100\pm10$ Å (area per macromonomer $2rh=250$ Å^2) and a height of 23 Å was found [17], a cylinder deformation as measured by curve ''*c*'' in Fig. 3(a).

The interfacial roughnesses or smearing parameters differ by a factor of about 3 ($\sigma_{air/pol}=3.3$ Å and $\sigma_{pol,w}=10\pm1$ Å); the polymer/air interface is much smoother. Comparison with the literature [38,39] shows that the roughness of the polymer/air interface can be explained by the thermally excited capillary waves at the water surface. In contrast, the high interfacial roughness $\sigma_{pol/w}$ is obviously caused by the swelling of the PVP side chains into the water. As will be shown below, the smooth polymer/air and the diffuse (and therefore rough) polymer/water interface is always found, independent of the structure of the thin film.

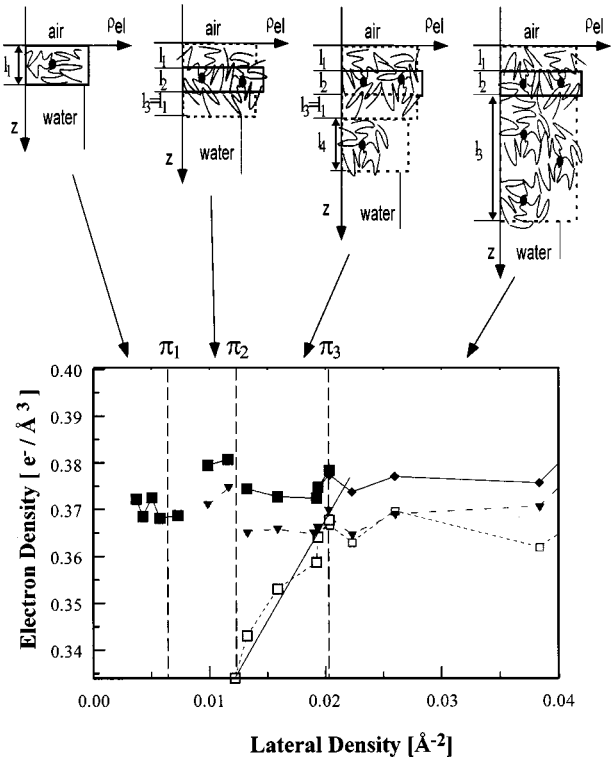

FIG. 5. Schematic view of the polymer in the different phases together with the parametrization according to the box model. Also shown is the electron density of the different slabs as a function of the lateral macromonomer density. Large full squares or diamonds correspond to the slab containing the cylinder core (beyond π_1, it is the second slab from the air side). Triangles correspond to the air-adjacent side chains, open squares correspond to the water-adjacent polymer layer (cf. Tables I–IV).

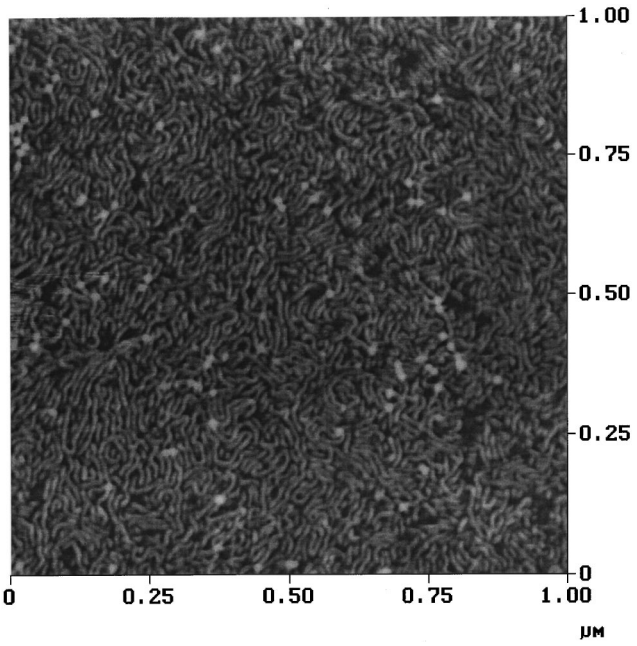

FIG. 6. AFM image of a monolayer transferred below π_1, transferred above π_1 did not yield any pattern (monolayer pressure 4.9 mN/m, transfer speed 1 cm/min, and transfer ratio 1).

Between π_1 and π_2 [curves ''*e*'' to ''*g*'' in Fig. 3(a)], the x-ray reflectivity curves get more and more structured. In ''*e*'' a second minimum appears, in ''*g*'' three maxima and two minima can be discerned. The one-box model used for the expanded phase below π_1 fails; the three-box model depicted in Fig. 5 is necessary to fit all data curves between π_1 and π_2 successfully. The thus obtained electron-density profile was identical to the one found by model independent inverse Fourier transformations [32,33]. Within this three-box model, the second box exhibits the highest electron density. It can be ascribed to the core of the ''cylindrical'' brush. To reduce the amount of free parameters, the first and third box are assumed to be identical (cf. Table II), a numerical approach that makes sense due to the structural symmetry of the cylindrical brush. Because the lengths of the three slabs describing the brush are independent, the sum $(2l_1+l_2)$ is the most reliable parameter of the fit. Basically, $(2l_1+l_2)$ is directly determined by the periodicity of the extrema in ''*f*'' and ''*g*''. The same low surface roughness $\sigma_{\mathrm{air/w}}$ as for the polymer/air interface is used for all inner interfaces. As mentioned before, a second substantially larger roughness $\sigma_{\mathrm{pol/w}}$ is necessary to describe the polymer/water interface. Between π_1 and π_2, the monolayer increases in thickness from about 30 to 50 Å [cf. Fig. 4(b)], while the area per macromonomer decreases to $2rh=2\times17\times2.5\,\text{Å}^2=85\,\text{Å}^2$. As can be seen in Fig. 4(a), the volume of a PVP macromonomer is not influenced by the phase transition at π_1. Thus the cross section of the ''cylindrical'' brushes is best described as a compressed ellipsoid.

C. The monolayer on solid substrates

The monolayer was transferred at various pressures onto silicon wavers and investigated with the atomic force miscroscope (AFM) in the tapping mode. A typical image of the ''cylindrical'' brushes transferred below π_1 is shown in Fig. 6, where isolated molecules can be distinguished. Locally, parallel orientation of the main chains does occur. A few hairpins are found. Obviously, the polymer/air interface is no longer the smooth homogeneous surface found on water, indicating dehydration and/or lateral shrinking on transfer.

TABLE II. Between π_1 and π_2 the electron-density profile of the laterally interacting monolayer is parametrized as a three-box model (cf. Fig. 5), where the first and third box are identical ($\rho_1=\rho_3$ and $l_1=l_3$). $G_{\mathrm{air/pol}}$ describes the roughness at the air/polymer interface as well as all the inner roughnesses. Again, $\sigma_{\mathrm{pol/w}}$ is the roughness at the polymer/water interface.

	Area (Å^2)	$l_1=l_3$ (Å)	$\rho_1/\rho_w=\rho_3/\rho_w$	l_2 (Å)	$\rho_2\rho_w$	σ (Å)	$\sigma_{\mathrm{pol/w}}$ (Å)	$l_{\mathrm{sum}}=2l_1+l_2$ (Å)
e	137.1	9.2	1.09	17.2	1.122	3.276	6.45	35.64
f	101.4	16.3	1.11	11.4	1.136	3.338	6.89	43.88
g	86.2	17.1	1.12	15.0	1.140	3.394	7.5	49.06

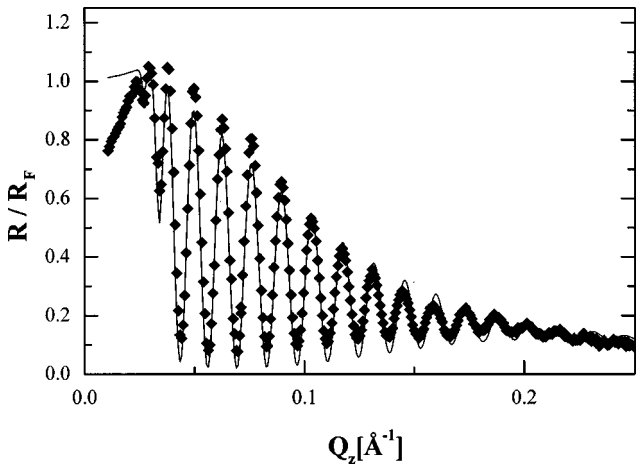

FIG. 7. Normalized x-ray reflectivity of 13 monolayers transferred at 18.1 mN/m onto a solid support.

This image is reminiscent of the spin-coated cylindrical brushes in [17], yet in our case the coverage was higher. It is very interesting to note that AFM images could only be obtained if the monolayer was transferred below π_1. Above π_1, with the onset of strong vertical deformation, the side chains of opposing cylindrical brushes touch and hinder any dehydration, and/or lateral shrinking is not pronounced enough to enable observation of lateral structure by AFM. Yet, at a pressure above π_1 it is possible to form multilayers from cylindrical brushes. As a typical example, Fig. 7 shows an x-ray reflectivity curve of 13 monolayers transferred slightly below π_2. Unfortunately, the spectrometer was to misaligned to determine the electron density. Still, a few interesting film properties can be deduced. There is no discernible structure within the polymer film; all measurements could be fitted by a one-box model with uniform thickness. As to be expected, the substrate/polymer roughness is determined by the silicon waver, $\sigma_{Si}=3.5$ Å. The thickness increase per transferred monolayer is 34.1 Å, a value that is further confirmed by frequent x-ray measurements during multilayer buildup. However, this value is considerably lower than the one obtained at the air/water interface, 44 Å, and is quantitatively consistent with complete dehydration of the monolayer during transfer.

D. Double-layer formation at the air/water interface

The phase transition at π_2 occurs at a molecular area of $\approx$85 Å^2, and is marked by a distinct knee in the isotherm. The x-ray reflectivity curves shown in Fig. 8 are structured, exhibiting between three and five maxima. Yet, on compression, no continuous shift of the minimum position to smaller Q_z occurs (different from the monolayer, cf. Fig. 3). Instead, on the shoulder of the first maximum, an additional maximum forms and grows during compression. Double-layer formation is almost completed at curve ''*j*''; then, the double layer thickens without pronounced structural changes. If one compares the compressed monolayer ''*g*'' and the compressed double layer ''*l*,'' one finds a doubling of the periodicity of the interference fringes corresponding to twice the film thickness.

During double-layer formation, the reflected signal is a superposition of the monolayer and double-layer reflectivities [38]. If the domains exceed the coherence length of the x rays (1 μm), the superposition occurs incoherently, which can be recognized by typical isosbestic points in the reflectivity curves. Yet, we found no isosbestic points; we measured the averaged electron-density profile obtained by laterally integrating over the monolayer and double layer. The coherent superposition we find indicates that the domains of the second layer are smaller than 1 μm and may be as small as a single cylindrical brush.

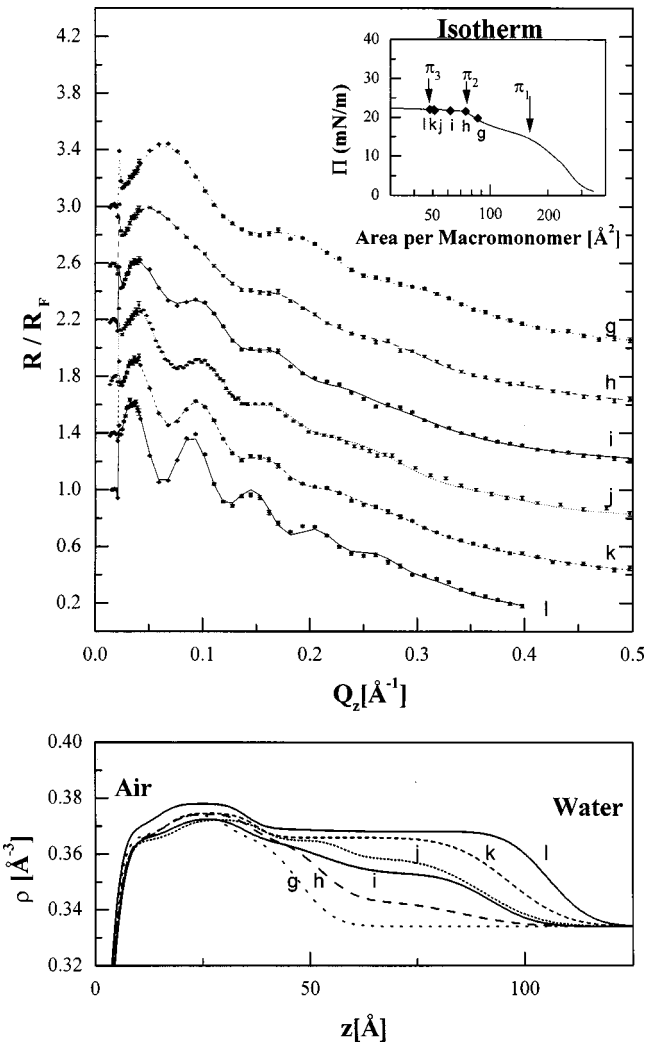

FIG. 8. Top: Normalized x-ray reflectivity during double-layer formation taken along the isotherm (shown in the inset) between π_2 and π_3. For clarity, each curve is displaced by 0.4. Bottom: The corresponding electron-density profiles.

The electron-density profiles derived from model-independent calculations exhibit a maximum density region some 20 Å away from the air/polymer interface. This region is significant; without it, the structure in the reflectivity curves beyond $Q_z=0.2$ Å^{-1} would disappear. The model with the least free parameters, which still succeeded in fitting all x-ray reflectivity curves between π_2 and π_3, is sketched in Fig. 5. Four boxes are necessary. Counting from the air, the first three boxes describe a monolayer of ''cylindrical'' brushes with the main chain lying parallel to the water surface. As before, the first and third box describing the shell of the ''cylindrical'' brush are assumed to be identical, while the second box for the cylinder core has the highest electron

TABLE III. Between π_2 and π_3 the electron-density profile of the forming double layer is parametrized as a four-box model (cf. Fig. 5), with identical first and third boxes ($\rho_1=\rho_3$ and $l_1=l_3$). The fourth box describes the growing bottom monolayer. $G_{\text{air/pol}}$ is the roughness at the air/polymer interface as well as all inner roughnesses; the one at the polymer/water interface is $\sigma_{\text{pol/w}}$. Just after π_2, an additional roughness $\sigma_{3,4}$ between boxes 3 and 4 is necessary.

	Area (Å^2)	$l_1=l_3$ (Å)	$\rho_1/\rho_w=\rho_3/\rho_w$	l_2 (Å)	ρ_2/ρ_w	$l_{\text{mono}}=2l_1+l_2$	σ (Å)	$\sigma_{3,4}$ (Å)	l_4 (Å)	ρ_4/ρ_w	$\sigma_{\text{pol/w}}$ (Å)	l_{sum} (Å)
h	75.57	16.55	1.094	19.22	1.121	52.32	3.745	6.482	33.12	1.027	11.16	85.44
i	62.97	18.05	1.095	16.26	1.116	52.36	3.93	9.35	39.51	1.057	8.361	91.87
j	51.97	19.19	1.092	19.5	1.115	57.88	3.814		32.42	1.074	10.58	90.30
k	51.62	17.34	1.096	19.16	1.122	53.84	3.725		42.26	1.09	9.835	96.30
l	49.13	14.94	1.107	19.25	1.133	49.13	3.508		56.4	1.101	7.678	105.53

density. The fourth box is ascribed to the growing second layer. The air/polymer roughness $\sigma_{\text{air/pol}}$ describes also the smearing of the interfaces between the different boxes, $\sigma_{\text{pol/wat}}$ the diffuse polymer/water interface. For curves ''*h*'' and ''*i*'', an additional roughness between boxes ''three'' and ''four'' was necessary. These are eight or nine free parameters, respectively (cf. Table III). Yet the measured curve is so complex that the description is unambiguous.

The analysis of the derived parameters shows interesting features. First of all, the model—one ''cylindrical'' brush layer adjacent to the air/interface—appears to be self-consistent; the monolayer thickness is found to be 53 ± 3 Å (cf. Table III), a value consistent with a laterally compressed ''cylindrical'' brush [cf. Fig. 4(b)].

As indicated by the electron-density profiles [cf. Fig. 8(bottom)], the second brush layer forms from the water side. On compression, its electron density increases monotonously from the water value towards the polymer value. During the growth of the bottom layer, its thickness is $\approx$35 Å, i.e., a factor 1.5 less than in the top layer. To explain it, one may assume a surface-induced lateral expansion of the bottom layer. An alternative explanation of the small double-layer thickness is the model of Sautter *et al.* [22], which describes the double layer buildup of parallel long-chain molecules by hexagonal stacking. In this model, the average double-layer thickness amounts to $d[1+\sin(60°)]=1.87d=86$ Å, with $d=46$ Å as thickness of the undeformed cylinders. This value is indeed very similar to the experimental thin-film thickness (89 Å); however, it is inconsistent with the thickened top and flattened bottom layer found experimentally. Within each layer the long-chain molecules are subject to pronounced and different deformation of their cross -section, which makes uncorrelated stacking likely.

When the electron density of the bottom monolayer approaches the one of the hydrated side chains, it starts to thicken too, until it is as compressed as the top monolayer. Yet, only for the top monolayer the cylinder core can be distinguished in the electron-density profile, indicating a less stratified structure of the bottom monolayer. Experimentally, for the last two measurements, *k* and *l*, it is impossible to distinguish the bottom monolayer from the PVP side chains of the top monolayer, and the three-box model shown in Fig. 5 (originally designed for pressures above π_3) is sufficient. The structural details of the bottom layer cannot be distinguished, presumably due to the softness of the bottom layer and diffuseness of the polymer/water interface.

E. Homogeneous thickness increase

In Fig. 9 the x-ray reflectivity measurements for pressures beyond π_3 are shown. While the lateral pressure increases only slightly, the tremendous thickness increase of the polymer layer is obvious by the increasing periodicity of the interference fringes. Yet, the surface layer is not homogeneous; the measurements cannot be described by a simple

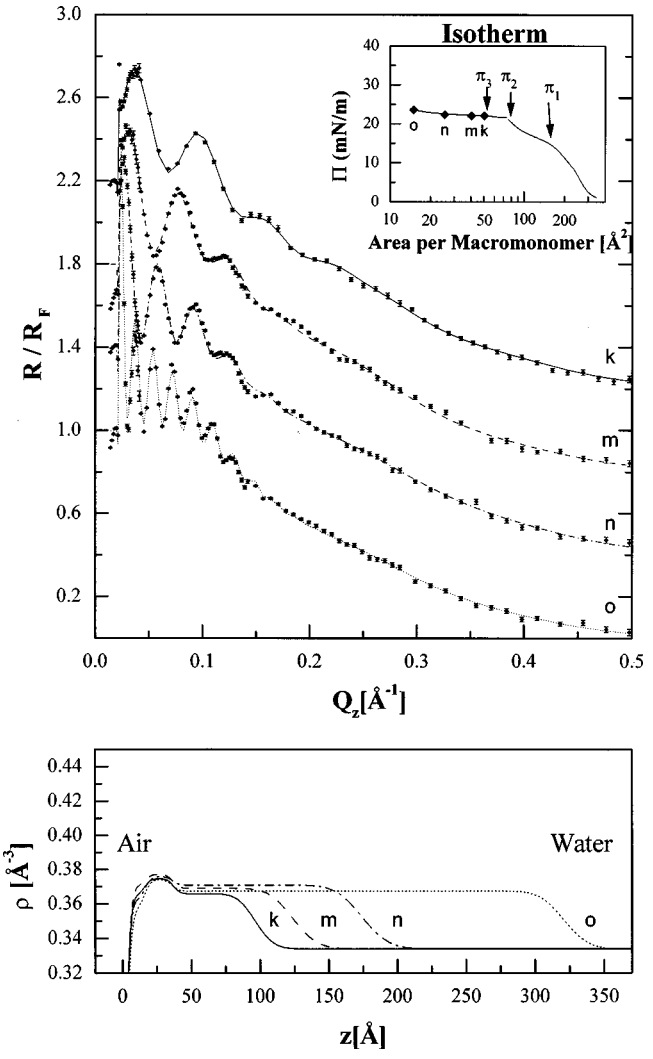

FIG. 9. Top: Normalized x-ray reflectivity during homogeneous film growth along the isotherm (shown in the inset) above π_3. For clarity, each curve is displaced by 0.4. Bottom: The corresponding electron-density profiles.

TABLE IV. Above π_3 the electron-density profile of the growing multilayer can be parametrized as a three-box moddel (cf. Fig. 5). $G_{\mathrm{air/pol}}$ is the roughness at the air/polymer interface as well as all the inner roughnesses; the one at the polymer/water interface is $\sigma_{\mathrm{pol/w}}$.

	Area (Å^2)	l_1 (Å)	ρ_1/ρ_w	l_2 (Å)	ρ_2/ρ_w	$l_{\mathrm{mono}}=2l_1+l_2$	l_3 (Å)	ρ_3/ρ_w	$\sigma_{\mathrm{pol/w}}$ (Å)	$l_{\mathrm{multi}}=l_{\mathrm{sum}}-l_{\mathrm{mono}}$	$G_{\mathrm{air/pol}}$
k	51.62	16.09	1.092	21.05	1.122	53.23	59.26	1.095	10.43	43.17	3.69
l	49.13	13.39	1.098	22.43	1.133	49.21	69.68	1.103	7.752	56.29	3.44
	44.88	14.19	1.087	21.89	1.119	50.27	72.7	1.092	9.34	58.51	3.67
m	38.49	16.09	1.107	20.45	1.129	52.63	87.06	1.105	13.94	70.97	3.79
	26.07	16.54	1.084	19.91	1.125	52.99	137.6	1.11	15.3	121.06	3.65
n	22.88	15.42	1.111	26.22	1.166	57.06	165.1	1.148	18.91	149.68	3.68
	19.69	17.25	1.088	19.13	1.144	53.63	214	1.139	16.46	196.75	3.78
o	15.25	15.88	1.065	20.25	1.12	52.01	284.6	1.1	13.84	268.72	3.92

one-slab model. For instance, the minima in ''*o*'' follow a rounded background. Consistent with the model-independent fits, the three-box model was chosen (cf. Fig. 5). Again, we find a region of maximum electron density 15–20 Å away from the air interface; to this region the second box is attributed. The first box is above the high electron-density region, the third one below. No explicit coupling between any of the boxes was introduced. The roughness of the polymer/air interface describes all inner interfaces, too. A second roughness is attributed to the polymer/water interface (cf. Table IV).

A top layer of compressed cylinders aligned parallel to the air/water interface is found, and a bottom layer of homogeneously distributed cylindrical brushes, which continuously thickens. To check the consistency of this model, the thickness of the air adjacent cylinders is calculated as a sum of the thickness of the second box, and twice the one of the first box. (This approximation is valid, since the second box corresponds to the cylinder core whose electron density is constant within error, cf. Fig. 5. Also, the electron density of the air adjacent side chains is constant.) As Figs. 9 and 10 show, the thickness of the top layer of ''cylindrical'' brushes is constant and identical to the one found during double-layer buildup. Since the thickness of the homogeneous multilayer increases linearly as a function of the inverse area per macromonomer, the hydrated volume can be calculated (4766 Å^3). Thus, one finds a higher degree of hydration than for the isolated monolayer, about 2.5 water molecules per pyridine monomer. Yet, the dry volume, 3230 Å^3 per macromonomer, is within 1% the same as the one calculated from the monolayer [cf. Figs. 4(a) and 10]. Note that the higher water content in the multilayer does not necessarily mean a higher PVP hydration. It is much more likely that the 11% volume increase (additional 18 water molecules per macromonomer) fills the space between the cylinders, since maximum close packing in three dimension is less efficient than in two dimensions.

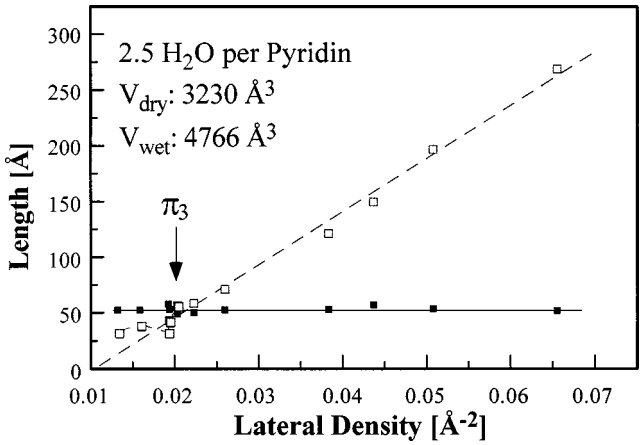

FIG. 10. The thickness of the top monolayer [full squares, cf. Fig. 3(a)] and of the bottom layer as a function of the lateral macromonomer density (open squares) (cf. Tables III and IV) both for double-layer buildup and homogeneous film growth, i.e., $\pi > \pi_2$.

The maximum film thickness experimentally achievable is about $l = 310$ Å (i.e., 10 Å^2/macromonomer); then the film kinetics is too slow to obtain equilibrium. Such a limiting thickness was expected since with increasing film thickness the glass-transition temperatures decreases. Approaching the glass transition causes a viscosity increase [26].

III. DISCUSSION

Since the volume per macromonomer is basically constant, the phases of a cylindrical brush film at the air/water interface can be described as wetting and layering transitions [cf. Figs. 4(a) and 10], even though the melt appears to be slightly more swollen than the monolayer, an effect probably due to less efficient volume filling of the long-chain particles in three dimensions. Before the layering transitions occur, the isotherm shows another phase transition at π_1, which has to be attributed to changes of the tethered side chains. Note that the point where the ''cylindrical'' brush actually exhibits a cylindrical geometry (i.e., $l_{\mathrm{mono}}=2l_1+l_2=2r=46.5$ Å) is not special in the isotherm [cf. Fig. 4(b)]. This indicates that interfacial interactions influence strongly the structure of the ''cylindrical'' brush monolayer. The impossibility to obtain AFM images above π_1 indicates that at this phase transition lateral interactions between the long-chain particles start to contribute strongly.

We have two different models to explain the phase transition at π_1. (i) The thickness at π_1, 30 Å, corresponds to, roughly, three cross-sectional areas of PVP chains. This suggests an adsorption transition of the tethered side chains, which leave the respective interfaces and are immersed in the cylindrical brush itself. In this picture, the phase transition would always occur at the same film thickness, independent

of side-chain length. (ii) π_1 can be seen as a transition from an expanded to a compressed state of the side chains, if and only if side chains cannot cross the main chain (i.e., each side chain is stuck at the right or left of the main chain). At π_1, the cylindrical brush radius equals the monolayer thickness [i.e., $r = 1_{\mathrm{mono}}$, cf. Fig. 4(b)], i.e., all side chains are confined to a volume of equal height and width. In this picture, longer side chains of the cylindrical brush would shift π_1 to a larger film thickness.

Finally, it is intriguing to observe that the numerical values of film thickness and radius at the first measurable pressure increase (15 and 55 Å) are almost identical to the radius and thickness of the most compressed monolayer (17 and 53 Å), indicating a limit to the deformation. In this picture the tethered side chains are confined to one side of the ''cylinder'' core.

Two layering transitions are observed; first, a double layer is formed, then the thickness of the bottom layer increases homogeneously. These layering transitions are similar to those observed in the melt of long-chain molecules [4,7] and can be explained in principle by the system topology [2]. The stratified top layer with the cylinder axis oriented parallel to the surface shows that the air/polymer interface is the smooth interface for the mesoscopic cylinders. This is consistent with the small air/polymer roughness compared to the water/polymer roughness. Yet, while layering is due to system topology, interfacial and intermolecular interactions cause the cylindrical brush to deform. During double- and multilayer formation, the top layer is laterally compressed, its thickness (52.6 Å) exceeds one of the undeformed cylinders (46.5 Å) by 13%. Cylinder deformation also occurs in the bottom layer. When the bottom layer nucleates, it is about 20% thinner (35 Å) than the undeformed cylinder. Very likely, the entropically favorable brush swelling causes this flattening.

On further double-layer compression, the bottom layer thickens. Note that the nucleating bottom layer is already more compressed than the isolated monolayer at π_1; thus we do not expect nor we find a side-chan phase transition within the bottom layer. The thicker bottom layer has to be due to the interlayer interactions, which balance the interfacial forces. Presumably, in the isotropic homogeneous multilayer, the cylindrical brushes are no longer deformed. This is a deceptively simple system, determined by a subtle balance between forces from two planar interfaces, intra- and intermolecular interactions that are all of comparable magnitude and can be varied in the experiment leading to different structures. From these, one can infer the effects of the acting forces.

(a) Dominant *intramolecular forces* would yield a constant diameter of the long-chain particles. The circular diameter ($2r = 46.5$ Å) of the ''cylindrical'' particles amounts to 75% of the side-chain contour length (62 Å), indicating a substantial stretching. Yet, no cylindrical symmetry is observed for the monolayer sandwiched between two interfaces, for the air/adjacent monolayer on top of a thin film, or for the bottom layer during double-layer growth. However, the intramolecular forces are sufficient to stretch the long-chain particle and lead to local in-plane alignment as observed with the AFM.

It is not yet clear if the monolayer transition at π_1 is due to intramolecular forces only, or if the interfacial forces contribute. This question could be answered by the use of different side-chain lengths or chemically different side chains.

(b) The *intermolecular forces* are mainly due to the steric repulsion of the tethered side chains. Obviously, the side chains do not interpenetrate and single particles can be distinguished. Indeed, the *structural forces* of purely geometric origin are strong enough to yield quasi-layering. Yet, the decay of the density oscillations perpendicular to the surface is very sudden; for the melt, only the first layer can be clearly distinguished. Also a transition to a triple layer does not exist. This suggests a rather long-range interparticle repulsion, no steep hard-wall potential as usually assumed when structural forces are considered. Also, the diffuseness of the polymer/water interface contributes to the sudden disappearance of quasilayering. However, a clear distinction between interparticle and intraparticle forces is difficult since the interparticle repulsion is expected to depend on the cylinder deformation. Further experiments have to clarify the influence of the side-chain length on the cylindrical brush softness.

(c) Independent of the film structure, we find a very low roughness at the *air/film interface* indicative of a high surface energy. Obviously, air is an even worse solvent for the side chains than water, and thus no side chains stick into the air. Additionally, we find that the top monolayer of both the double-layer and the homogeneous film is laterally compressed; hence, the contact of the side chains with each other is increased and with water reduced. This deformation is more evidence for the bad solvent quality of water.

(d) Since spreading is observed, the *water/film interface* has to have a low surface energy. Obviously, the swelling of the PVP side chains manifested as the diffuseness of the particle/water interface causes a gain in entropy and free energy. The diffuseness seems to increase slightly on film compression. For the monolayer at zero pressure, the laterally expanding forces of the water/film interface exceed the laterally compressing forces from the air/film interface leading to a flat conformation (centipede with all legs spread). Also, during double-layer formation, the bottom monolayer is found to be flattened. It is likely that in the homogeneous film the particles on the water surface are still flattened, yet this is beyond the experimental resolution.

We would like to note that the formation of the second monolayer on the water side is rather unusual. Most other monolayers form three-dimensional structures towards the air (alcanes, dendrimers [40], and liquid crystals [10,16]). Yet the lung surfactant [41] goes into solution, a topic of intensive current research (the lung surfactant forms a monolayer, which separates the aqueous phase from the gaseous phase in the lung avioli. On breathing, the surface area is contracted and expanded by a factor of two, while the lateral density of the surfactant is maintained constant. Apparently, this is achieved by reversible multilayer growth into the solution). We can only speculate that in the case of the cylindrical brushes their hydrophilic nature causes this unusual behavior. Yet, we now have the chance to check theoretical predictions that domains growing on the water side should be smaller. The argument is based on the domain line tension, which needs to be overcome on domain nucleation [42,43]. Due to the difference in dielectric constants of the surrounding media, the line tension is one to two orders of magnitude

larger on the air side than on the water side [2]. Indeed, air-adjacent domains are μm sized, and can be observed optically [10]. Any domains growing at the water side should be much smaller; however, experimental evidence is still lacking. We can give a maximum domain size (1 μm), yet cannot exclude the nucleation of the second layer by single cylindrical chains [22].

CONCLUSION

The wetting of a cylindrical brush as a model system for soft long-chain mesoscopic particles was studied. The degree of hydration and thus the volume of the cylindrical brush is constant, both for the top monolayer and for the cylindrical brush melt. Therefore, our findings are described in the framework of polymer wetting. At first glance, this simple system is determined by a subtle balance between forces from two planar interfaces, intra-and intermolecular interactions that are all of comparable magnitude and can be varied in the experiment leading to different structures.

At low coverage, a monolayer is formed. Even though the ''cylinder'' radius amounts to 75% of the side-chain contour length, indicating substantial side-chain stretching, the monolayer is found to be very soft and easily deformed. On compression, its thickness increases from 15 to 53 Å, while the lateral ''cylinder'' radius decreases from 55 to 17 Å. Furthermore, a phase transition occurs within the monolayer, which is tentatively attributed to a change of the side chains from a flattened to a compressed state. In spite of the particle softness, AFM images of the monolayer transferred onto Si wavers show local alignment and a large persistence length. Two layering transitions of the long-chain particles are observed, one from the monolayer to the double layer, the next to an unstructured multilayer. The surface energy of the air/polymer interface is high, causing a very smooth and hard interface ($\sigma_{\mathrm{air/pol}} \approx 3.5$ Å). Therefore, surface layering starts from there, and during double- and multilayer formation, the top monolayer is well defined, with the ''cylinder'' axis parallel to the surface and in a laterally compressed state (13%), the latter effect is attributed to the bad solvent quality of water. In contrast, the particle/water interface is diffuse ($\sigma_{\mathrm{pol/w}} \approx 10$ Å) indicating brush swelling. The entropy and free-energy gain from the particle/water interface appears to favor a flat conformation of the ''cylindrical'' brushes in the bottom layer. Experimentally, this flattening is observed when the second layer nucleates at the water side.

In conclusion, while in most phases the circular diameter of the particles adjacent to the respective interfaces is not maintained, the structural forces of purely geometric origin are still strong enough to cause layering transitions and a structured density profile adjacent to the hard wall. Yet, deviations from layering as described for hard long-chain molecules are found. There is no transition from a double to a triple layer. Also, the quasilayering in the density profile of the melt does not decay gradually; only the top layer can be distinguished. These deviations are attributed to the long-chain particle softness together with the long range of the interparticle forces.

ACKNOWLEDGMENTS

The comments of Helmuth Möhwald, Werner Göedel, Karl Fischer, Diethelm Johannsmann, and Wolfgang Schärtl improved the manuscript. The financial support of the Schwerpunkt ''Benetzung'' (He 1616/9-1,2) and the SFB 262 is gratefully acknowledged, as well as the contributions of the MWFZ and the Fond der Chemie.

[1] M. Muthukumar, C. K. Ober, and E. L. Thomas, Science **277**, 1225 (1997).
[2] J. N. Israelachvili, *Intermolecular and Surface Forces* (Academic, London, 1991).
[3] O. M. Magnusson, B. M. Ocko, M. J. Regan, K. Penanen, P. S. Pershan, and M. Deutsch, Phys. Rev. Lett. **74**, 4444 (1995).
[4] R. Horn and J. N. Israelachvili, Macromolecules **21**, 2836 (1998).
[5] A. v. Blaaderen and P. Wiltzius, Science **270**, 1177 (1995).
[6] H. Löwen and M. Schmidt, in *Progress in Colloid and Interface Sciences*, edited by F. Kremer and G. Lagaly (Steinkopf Verlag, Darmstadt, Germany, 1997).
[7] P. G. d. Gennes and A. M. Cazabat, C. R. Acad. Sci., Ser. II: Mec. Phys., Chim., Sci. Terre Univers. **310**, 1601 (1990).
[8] P. A. Thompson, G. S. Grest, and M. O. Robbins, Phys. Rev. Lett. **68**, 3448 (1992).
[9] M. Schoen, S. Hess, and J. Diestler, Phys. Rev. E **52**, 2587 (1995).
[10] M. Harke, M. Ibn-Elhaj, H. Möhwald, and H. Motschmann, Phys. Rev. E **57**, 1806 (1998).
[11] M. J. Regan, E. H. Kawamoto, P. S. Pershan, N. Maskil, M. Deutsch, O. M. Magnussion, B. M. Ocko, and L. E. Perman, Phys. Rev. Lett. **75**, 2498 (1995).
[12] P. Lang, C. Braun, R. Steitz, G. H. Findenegg, and H. Rahn, J. Phys. Chem. B **102**, 7590 (1998).
[13] G. Cevc, W. Fenz, and L. Sigl, Science **249**, 1161 (1990).
[14] J. Als-Nielsen, in *Structure and Dynamics of Surfaces*, edited by W. Blanckenhagen (Springer, New York, 1986).
[15] S. P. Weinbach, K. Kjaer, W. Bouwman, J. Als-Nielsen, and L. Leiserowitz, J. Phys. Chem. **100**, 8256 (1996).
[16] M. Ibn-Elhaj, H. Riegler, H. Möhwald, M. Schwendler, and C. A. Helm, Phys. Rev. E **56**, 1844 (1997).
[17] P. Dziezok, S. S. Sheiko, K. Fischer, M. Schmidt, and M. Möller, Angew. Chem. Int. Ed. Engl. **36**, 2812 (1997).
[18] V. Percec, C. Ahn, G. Ungar, D. J. P. Yeardlag, and M. Möller, Nature (London) **391**, 161 (1998).
[19] J. Roovers, L. L. Zhou, P. W. Toporowski, M. v. d. Zwan, H. Iatrou, and N. Hadjichristidis, Macromolecules **26**, 4234 (1993).
[20] P. G. deGennes in *Advances in Polymers Science*, edited by S. Granick (Springer, Berlin, 1998), Vol. 138.
[21] B. Rapp and H. Gruler, Phys. Rev. A **42**, 2215 (1990).
[22] E. Sautter, S. I. Belousov, W. Pechhold, N. N. Makarova, and Y. K. Godovsky, Vysokomol. Soedin., Ser. A Ser. B **38**, 49 (1996).
[23] C. A. Helm, H. Möhwald, K. Kjaer, and J. Als-Nielsen, Europhys. Lett. **4**, 697 (1987).
[24] L. Bosio, J. J. Benattar, and F. Rieutord, Rev. Phys. Appl. **22**, 775 (1987).

[25] G. Gabrielli, Colloid Polym. Sci. **261**, 82 (1983).
[26] J. D. Ferry, *Properties of Polymers* (Wiley, New York, 1980).
[27] B. Jérôme and J. Commandeur, Nature (London) **386**, 589 (1997).
[28] H. Baltes, M. Schwendler, C. A. Helm, and H. Möhwald, J. Colloid Interface Sci. **178**, 135 (1996).
[29] P. S. Pershan, Faraday Discuss. Chem. Soc. **89**, 231 (1990).
[30] I. M. Tidswell, B. M. Ocko, P. S. Pershan, S. R. Wasserman, G. M. Whitesides, and J. D. Axe, Phys. Rev. B **41**, 1111 (1990).
[31] A. Asmussen and H. Riegler, J. Chem. Phys. **104**, 8159 (1996).
[32] J. S. Pederson, J. Appl. Crystallogr. **25**, 129 (1992).
[33] J. S. Pederson and I. W. Hamley, J. Appl. Crystallogr. **27**, 36 (1994).
[34] O. Albrecht, H. Gruler, and E. Sackmann, J. Phys. (Paris) **39**, 301 (1978).
[35] S. I. Belousov, E. Sautter, Y. K. Godovsky, N. I. Makarova, and W. Pechhold, Vysokomol. Soedin., Ser. A Ser. B **38**, 1532 (1996).
[36] E. Pretel, Macromolecules **30**, 2775 (1997).
[37] E. Donath, D. Walter, V. N. Shilov, E. Knippel, A. Budde, K. Lowack, C. A. Helm, and H. Möhwald, Langmuir **13**, 5294 (1997).
[38] C. A. Helm, P. Tippmann-Krayer, H. Möhwald, J. Als-Nielsen, and K. Kjaer, Biophys. J. **60**, 1457 (1991).
[39] M. L. Schlossmann, D. K. Schwartz, P. S. Pershan, E. H. Kawamoto, G. J. Kellog, and S. Lee, Phys. Rev. Lett. **66**, 1599 (1991).
[40] S. S. Sheiko, A. M. Muzafaorv, R. G. Winkler, E. V. Getmanova, G. Eckert, and P. Reineker, Langmuir **13**, 4172 (1997).
[41] M. M. Lipp, K. Y. C. Lee, D. Y. Takamoto, J. Zasadzinski, and A. J. Warrig, Phys. Rev. Lett. **81**, 1650 (1998).
[42] D. J. Benvegnu and H. M. McConnell, J. Phys. Chem. **97**, 6686 (1993).
[43] C. A. Helm and H. Möhwald, J. Phys. Chem. **92**, 1262 (1988).